Numerical Investigation of Turbulent Flow around an Obstacle: Effects of Inclination Angle on Flow Dynamics

NORA BENSIDER, AMINA MATAOUI, SAMIRA HAMAILI LOUAIFI
Theoretical and Applied Fluid Mechanics Laboratory,
Université des Sciences et de la Technologie Houari Boumediene USTHB,
BP 32, 16111, USTHB, Algiers,
ALGERIA

Abstract:-This paper proposes a numerical study of a turbulent flow around an inclined square obstacle in a channel. The objective of this work is to examine the effect of the obstacle inclination (θ) on the boundary layer separation. The two-dimensional unsteady Reynolds-averaged Navier-Stokes equations (2D-URANS) were solved by the finite volume method using the shear stress transport k-ω model ((SST-(k-ω)) for turbulence closure. Validation is carried out with available experimental data and large eddy simulation (LES) results of the no inclined case (θ=0◦). Six obstacle inclinations in the range 0∘ ≤θ≤45 ∘, for Reynolds number Re=3000, are examined. The results show that the Strouhal number (St) increases linearly until it reaches a maximum value (St = 0.145) for a critical angle (θ = 15°), then decreases below this value.

Key-Words: - Obstacle inclination, Von Kármán vortex shedding, Strouhal Number, CFD, Finite volume method, Turbulence.

Received: July 8, 2025. Revised: October 19, 2025. Accepted: November 9, 2025. Published: December 31, 2025.

1 Introduction

Turbulent flows around obstacles are considered as a fundamental problem of fluid mechanics and are widely encountered usually in industrial applications, including: aerodynamics, building design, and electronic devices.The study of the vortex structures generated by these flow configurations is required to explain their flow behavior. Different studies on this type of flow configuration are available in the scientific literature, [1], [2], [3], which have explained the mechanism of vortex generation and flow separation for a similar case of flow configurations.

The prediction of turbulent behaviors of flow separation zones around obstacles is a main topic of industrial applications. While some studies, [4], clarify the discrepancy of eddy viscosity values between RANS and LES models. The present study validates the efficiency of the SST-(k-ω) model for similar configurations.

Several experimental studies have been conducted to explain turbulence instabilities surrounding obstacles. Among them, the investigation of [5], carried out on unstable turbulence near a rectangular cylinder in channel flow using Laser Doppler Velocimetry (LDV). They measured time-averaged and phase-averaged statistics for cylinders of different height-to-width ratios (b/h). They revealed that the maximum intensity of disturbances is reached near the stagnation point downstream of the recirculation zone.

Furthermore, [6], simulated by Large Eddy Simulation (LES) the vortex structures induced by turbulent flow around a confined square cylinder in a channel for a Reynolds number of 3000 and an obstruction ratio of 20%, and they examined the turbulent flow structure. They compared mean velocity profiles, turbulent fluctuations, Reynolds stresses, contours of turbulent fluctuations, and turbulence intensity with available experimental results.

The Kármán vortex shedding was also obtained. The predicted results were consistent with the experimental data reported in [5]. The study [7] simulated by large eddy simulation (LES) three-dimensional flow around unmoving bodies, focusing on a square cylinder (case A) and a wall-mounted cube (case B). For case A, the experimental results evidence an unsteady flow regime characterized by a periodic behavior. Instantaneous flow visualizations were used to investigate the flow dynamics; the flow conditions selected for their simulations are obtained from those proposed in [8].

The study [9] carried out an experiment to examine the flow field structure around three-dimensional obstacles of different aspect ratios. They conclude that the flow structure around the obstacle depends on aspect ratio, angle of attack, Reynolds number, and the type of boundary layer. The study [10] investigated a fully developed turbulent flow through a matrix of cubes using Large Eddy Simulation (LES) and Reynolds-Averaged Navier-Stokes (RANS) approaches. A comparison of the predicted outcomes for mean flow and turbulence with relevant experimental data showed that the RANS approaches were able to reasonably predict the primary characteristics of the flow around a cube array.

The experimental study conducted in [11] on flow around square and cylindrical obstacles yielded significant findings. The shape of the obstacle influences the flow structure. Square obstacles produce more important turbulent effects than cylindrical ones, and generate larger low-pressure regions, whereas cylindrical obstacles exhibit a more uniform pressure distribution. In addition, the lift force applied to a square obstacle is greater than that of a cylindrical obstacle, which may have valuable consequences for engineering design. The study [12] analyzed URANS simulations of flow around a square cylinder, comparing diverse RANS turbulence models. They obtain the best agreement with experimental data by the SST-(k−ω) model. They also investigated the impact of corner cut-offs on flow characteristics, revealing important modifications in the near-surface flow structure around the cylinder.

A significant number of numerical and experimental studies have been conducted on flows in the region of obstacles. But a small number of studies have investigated the effect of obstacle inclination. Among them, [13] examined the laminar flow around an inclined square cylinder. They investigated the influence of the angle of incidence and Reynolds number on the forces applied to the obstacle. They identified the critical Reynolds number for vortex shedding and classified the observed flow patterns.

The results demonstrate that the angle of incidence strongly affects the location of the separation point and the wake structure. The study [14] has focused on analyzing turbulent flow around obstacles, examining how variations in obstacle geometry, particularly inclined edges, influence the flow behavior. Their work shows the significant influence of geometric parameters on turbulence and flow separation behaviors, providing useful information for engineering applications using fluid-structure interactions.

For this, a numerical study is performed on the influence of obstacle inclination. The effect of obstacle inclination is checked. Unsteady flow fields are found in good agreement with available experimental and numerical studies.

The present study investigates numerically the influence of obstacle inclination on the wake dynamics. Simulations are performed using the two-dimensional Unsteady Reynolds-Averaged Navier–Stokes (2D-URANS) equations using SST-(*k–ω)* turbulence model. This model is validated with benchmark experimental data and computed values by Large Eddy Simulation (LES) of [6]. The results show that the unsteady flow fields are in good agreement with the literature, confirming the consistency of adopting this approach for the present flow configurations.

The key contributions of this work are:

1. We perform a numerical study of inclined obstacles at different angles (from 0° to 45°) using 2D-URANS simulations with SST-(*k–ω)* turbulence modeling.
2. The methodology is validated with available experimental and numerical results, confirming the accuracy of velocity profiles and lift force evolution.
3. The effect of inclination on different variables is deepened through mean axial velocity profiles, vorticity contours, pressure distributions, and Strouhal number variations.

Paper organization: In Section 2, the governing equations, numerical procedure, and boundary conditions are presented. Section 3 discusses the results and compares them with previous work. In Section 4, we conclude the results of this work and present some perspectives and recommendations.

2 Methodology

2.1 Governing Equations

One investigates an unsteady two-dimensional flow of water, assumed to be incompressible and isothermal with constant physical properties. The averaged equations of motion (2D-URANS) are deduced from the continuity (equation (1)) and momentum (equation (2)):

$$\frac{\partial U_i}{\partial x_i} = 0 \quad (1)$$

$$\frac{\partial U_i}{\partial t} + U_j \frac{\partial U_i}{\partial x_j} = -\frac{\partial}{\partial x_i}\left(\frac{P}{\rho}\right) + \frac{\partial}{\partial x_j}\left(\nu \frac{\partial U_i}{\partial x_j} - \overline{u_i u_j}\right) \quad (2)$$

Three URANS turbulence models are tested for turbulence closure: two first-order models: the standard k–ε, [15] and SST-(k-ω), [16], [17], and the second-order Reynolds stress model. The k–ε model is based on the Prandtl–Kolmogorov eddy viscosity, which is quite accurate for high Reynolds numbers. While the SST-(k-ω) model, [16], [17], combines the k–ω model in the boundary layer and the k–ε model beyond the boundary layer. These two models require an additional cross-diffusion term in the dissipation rate equation. For first-order models, the Reynolds stresses are deduced from the Boussinesq equation as follows (Eq. (3)):

$$\rho\overline{u_i u_j} = \frac{2}{3}\rho k\delta_{ij} - \mu_t\left(\frac{\partial U_i}{\partial x_j} + \frac{\partial U_j}{\partial x_i}\right) \qquad (3)$$

The Reynolds stress model (RSM), [18], is a second-order turbulence model. It is based on transport equations for each Reynolds stress tensor component, coupled with the dissipation rate ε equation.

2.2 Numerical Procedure

The numerical prediction is performed by CFD software ANSYS FLUENT 14.0. The finite volume method, [19], requires a conservative formulation for all equations in terms of convection, diffusion, and source (Eq. (4)):

$$\frac{\partial}{\partial t}(\rho\phi) + \mathrm{div}(\rho\phi\mathbf{u}) = \mathrm{div}(\Gamma_\phi\,\mathrm{grad}\,\phi) + S_\phi \qquad (4)$$

where Φ is one of the dependent variables of this problem (U, V, k, and ω or ε), Γ_ϕ and S_ϕ correspond to the diffusion coefficient and source terms of each equation, respectively.

Spatial discretization is performed on collocated meshes. For interpolation SECOND-ORDER scheme is used for the convection-diffusion terms of velocity components and turbulent quantities. The PRESTO scheme is implemented for pressure. The SIMPLE algorithm is applied for pressure-velocity coupling.

2.2.1 Boundary Conditions

Figure 1 depicts the coordinate system and geometry. Different boundary conditions are implemented to accurately define the flow field through the computational domain. Inlet conditions are based on inlet velocity U_m=0.3 m/s, turbulent intensity 6% and hydraulic diameter (H).

The geometrical and dynamical parameters include a rectangular channel of length L of 0.5 m and height H of 0.05 m, and the square obstacle of side length h of 0.01 m. Reynolds number, Re, is based on the obstacle side length h and the inlet velocity, Um is 3000. Different inclinations of the obstacle were tested, ranging from 0° to 45°.

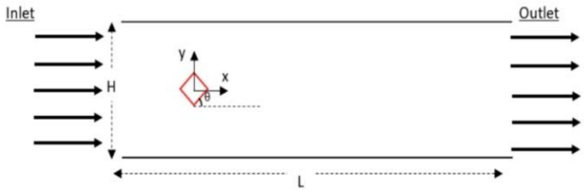

Fig. 1: Flow configuration
Source: created by the authors

2.2.2 Grid Arrangement and Time Step

Structured and non-uniform grids are generated with refinement surrounding a square obstacle. Figure 2 depicts the computational domain and grid configuration. Furthermore, thinning meshes are implemented near each wall to compute accurately gradients of all variables in particularly within the viscous sub-layer.

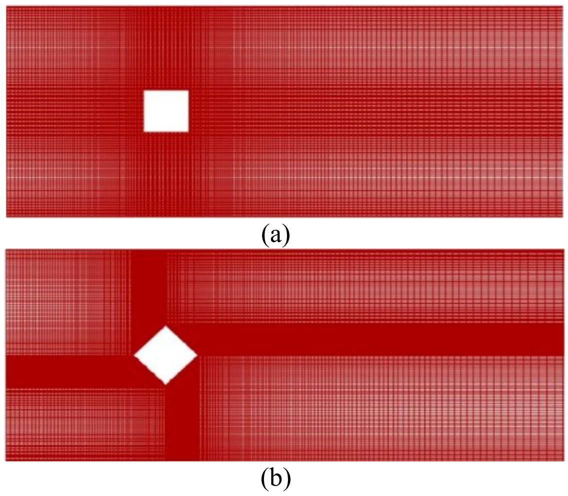

Fig. 2: Typical grid arrangement and computational domain (a) θ = 0° (b) θ = 45°
Source: created by the authors

We are examining different grids in order to choose the most appropriate one. A typical grid test is illustrated in Figure 3. However, the comparison to the experimental data of [5], and LES of [6], the third grid (mesh 2) offers an accurate numerical axial velocity prediction. Therefore, this grid is selected because it gives a good agreement and saves computational time.

Due to the slow oscillation of these flow configurations, a first-order method is used for all temporal interpolations with small time increments to achieve high accuracy.

Moreover, for a given time step of 0.005 s, the current number is equal to one for each inclination.

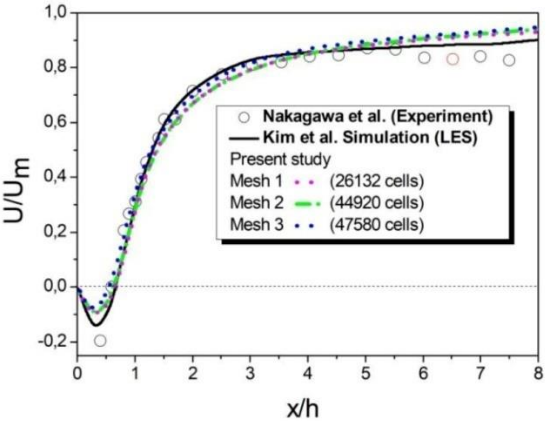

Fig. 3: Grid test (θ=0°)
Source: created by the authors

The validation was achieved with available experimental data in [5], and numerical results in [6]. This validation was performed for a no-inclined obstacle (θ=0°). The present results showed that the SST-(k-ω) first-order model accurately predicts the mean velocity profiles along the centerline (Figure 4) with the best precision compared to the other models (standard k-ε and RSM).An error analysis of longitudinal velocity is presented in Table 1, as an example. The error is computed following equation (5):

$$\varepsilon_r = \frac{\left|U_{Present} - U_{\exp}\right|}{U_{\exp}} \times 100$$

(5)

- The SST-(k–ω) model shows excellent accuracy along the centerline, with errors even in the recirculation zone.
- The RSM gives acceptable results, but is found slightly less accurate.
- The k–ε standard gives a significant deviation, confirming that it is not very suitable for this type of flow configuration. Furthermore, [20] demonstrated that the SST-(k-ω) model is more appropriate for problems generating vortex-induced vibrations. This result also confirms the efficiency of the SST-(k−ω) model for these types of flow configuration.

Table 1. Error analysis of longitudinal velocity

	ε_r %		
x/h	k-ε	RSM	*SST- (k-ω)*
1	80	20	3
2	44.4	6.7	2.2
3	30.8	3.1	1.5
4	26.7	2.7	1.3
5	25	2.5	1.3
6	15.7	2.4	1.2
7	15.3	2.4	1.2

Source: created by the authors

A further validation is conducted for θ=0° throughout the mean velocity components (U/Um (Figure 5) and V/Um (Figure 6)) along several cross-sections x/h = 1, 3.5, 6, and8.5).

Due to the symmetry with respect to the y-axis of the flow configuration, only half of the profiles are presented. The present results (in blue color) show an excellent agreement with available experimental data of [5], (in black color), and Large eddy simulation (LES) computed results of [6] (in grey color).

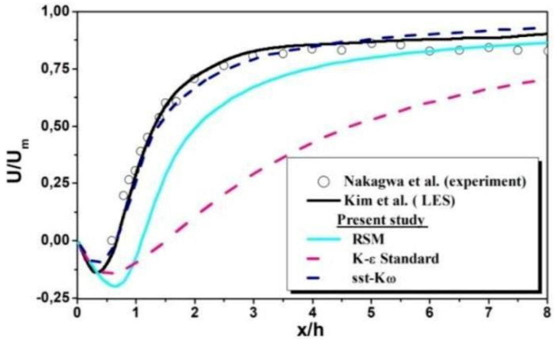

Fig. 4: Mean longitudinal velocity profile along the centerline (θ=0°)
Source: created by the authors

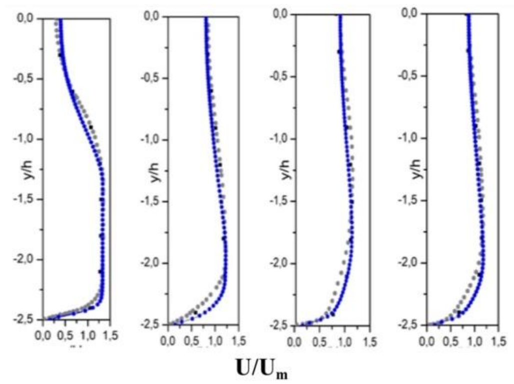

Fig. 5: Profiles of mean longitudinal velocity U/Um for θ=0° at x/h=1;3.5 ;6 and 8.5
Source: created by the authors

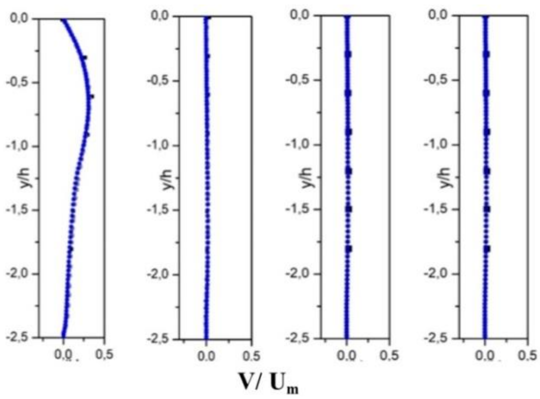

Fig. 6: Mean perpendicular velocity profiles V/Um for θ=0° at: x/h= 1;3.5 ;6 and 8.5

Source: created by the authors

3 Results and Discussions

3.1 Axial Velocity Profiles versus Inclination

Figure 7 represents the axial velocity profiles at x/h=30 downstream of the obstacle for different angles of inclination. In the case of no inclined obstacle (θ=0°), the flow is fully developed. Velocity profiles exhibit a flattened shape, characterizing a fully developed 2D channel flow. At θ = 10°, a small asymmetry induces a moderate deformation of the profile. At θ = 15°, the profile is very deformed due to the asymmetric recirculation zones. For θ=22.5°, the deformation reduces and the profile is close to that obtained at θ=10°. For θ=30°, the velocity distribution is like to that of the case where the obstacle is not inclined (θ = 0°). Finally, at θ=45°, the profile becomes quasi-parabolic, characterizing a more stable flow.

Moreover, Figure 7 also illustrates the axial velocity profile for x/h=30, downstream of the obstacle, evidencing a notable development of the turbulent flow behavior for different obstacle inclinations.

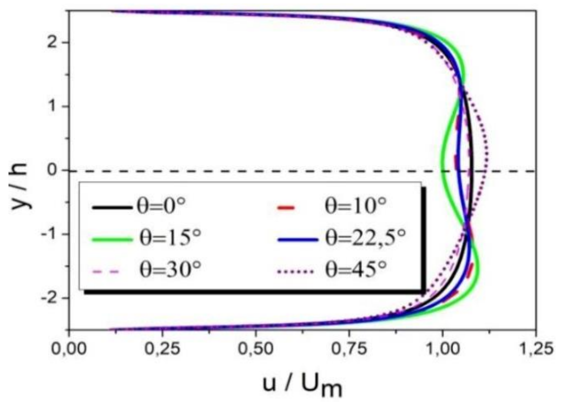

Fig. 7: Axial velocity profile for different inclination angles at x/h =30
Source: created by the authors

3.2 Contours Analysis of Vorticity Distribution

In Figure 8, qualitative analysis of the dimensionless vorticity contours for different obstacle inclinations confirms the influence of inclination on turbulence development and vortex formation. At an inclination of 15°, the vorticity contours are distorted and the flow becomes more asymmetrical. As the inclination increases, these contours tend to stabilise, leading to a gradual stabilisation of the flow and a reduction in the effects of turbulence.

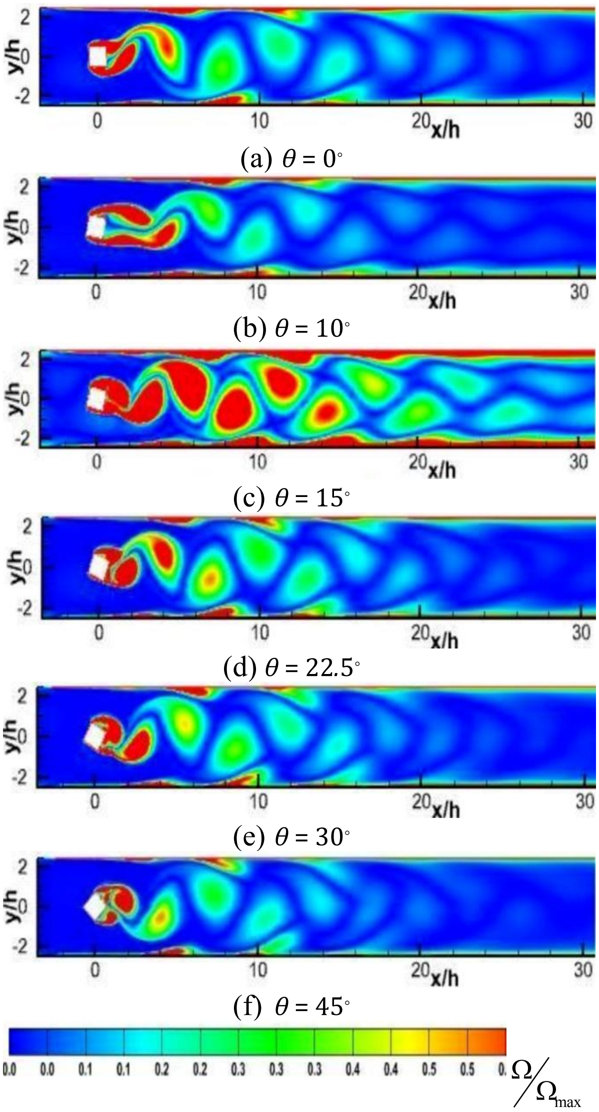

Fig. 8: Computed contours of normalized vorticity
Source: created by the authors

3.3 Pressure profiles versus obstacle inclination

Figure 9 represents the static pressure profiles at x/h =30 along the y-axis, for each inclination of the obstacle. When the obstacle is not inclined (θ = 0°), the pressure distribution is symmetrical. A very small effect appears for θ=10°, whereas at θ = 15°, the pressure distribution reaches its maximum due to a high level of asymmetry. When θ = 22.5°, the behaviour becomes more stable again, as in the case of θ = 10°. At θ=30°, the decrease in pressure is a sign of a reduction in turbulence. Finally, at θ=45°, the pressure is very low, indicating a more stable, symmetrical, and slightly disturbed flow.

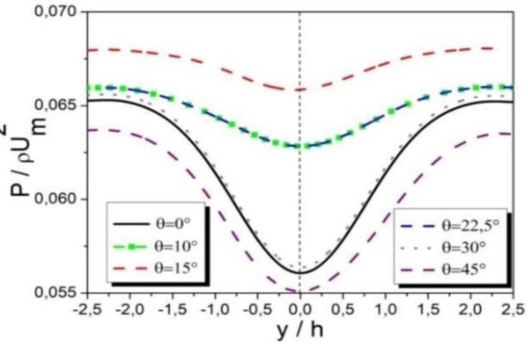

Fig. 9: Effect of obstacle inclination on static pressure profiles at x/h =30
Source: created by the authors

3.3.1 Time Analysis of the Lift Coefficient

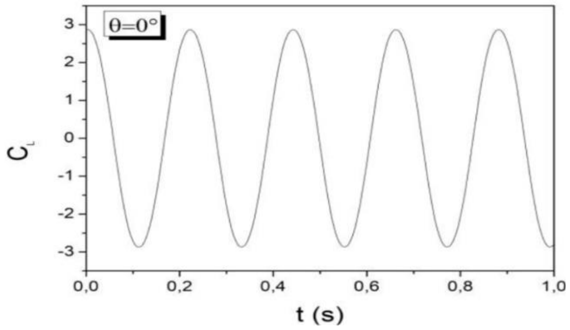

(a) $\theta = 0°$

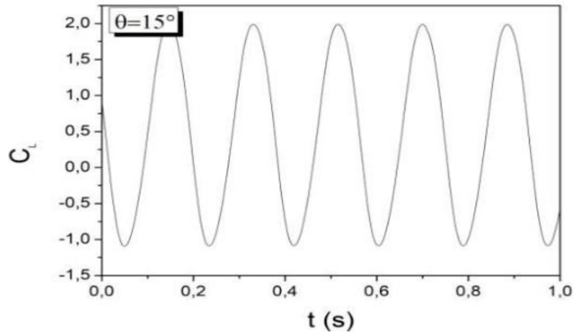

(b) θ =15° 15

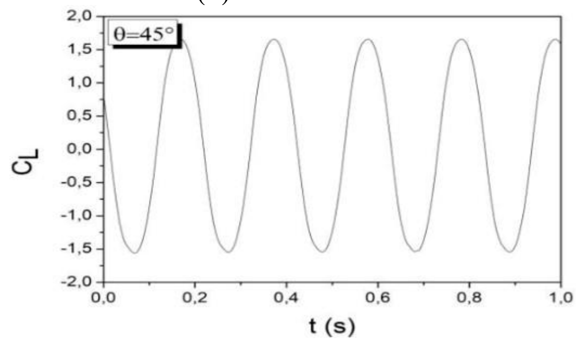

(c) $\theta = 45°$

Fig. 10: Time evolution of the lift coefficient for different inclinations
Source: created by the authors

The evolution of the lift coefficient for different inclination angles of θ=0°, θ=15°, and θ=45° (Figure 10a, Figure 10b, and Figure 10c) shows periodic oscillations, which confirms the unsteady behavior of the flow. The dominant frequency of each inclination was deduced from the temporal variation of the lift coefficient (Figure 11, Appendix).

Figure 12 (Appendix) shows the Strouhal number, deduced from the lift force frequency, the cylinder height (h), and the mean longitudinal velocity at the cylinder location U_b. Strouhal number (St) increases with obstacle inclination up to θ=15°, then begins to decrease beyond this angle.

Table 2 provides a summary for each inclination angle, presenting the mean longitudinal velocity at the cylinder's location (U_b) and the corresponding vortex shedding frequency (f).

Table 2. Strouhal number versus inclination

θ (°)	f (Hz)	U_b (m/s)	St
0	4.65	0.375	0.124
10	5.07	0.367	0.138
15	5.52	0.380	0.145
22.5	5.04	0.365	0.138
30	5.08	0.390	0.130
45	4.90	0.418	0.117

Source: created by the authors

3.4 Influence of Obstacle Inclination on Strouhal Number

Table 3 shows the Strouhal number (St) variation versus obstacle inclination. This allows for a clear observation of how the Strouhal number evolves with the obstacle's inclination. Maximal value is observed for the case θ=15°, corresponding to the more disturbed flow.

Table 3. Variation of the Strouhal number versus obstacle inclination

θ (°)	0	10	15	22.5	30	45
St	0.124	0.138	0.145	0.138	0.130	0.117

Source: created by the authors

Figure 13 clearly shows the influence of the Strouhal number (St) on the obstacle inclination. It increases practically linearly from θ=0° until θ=15°, reaching a maximum value at this critical point. Beyond θ=15°, it decreases almost linearly until θ=45°. This evolution follows two almost linear variations: an upward phase for small angles and a downward phase for higher obstacle inclination, which directly reflects changes in the vortex dynamics around the obstacle.

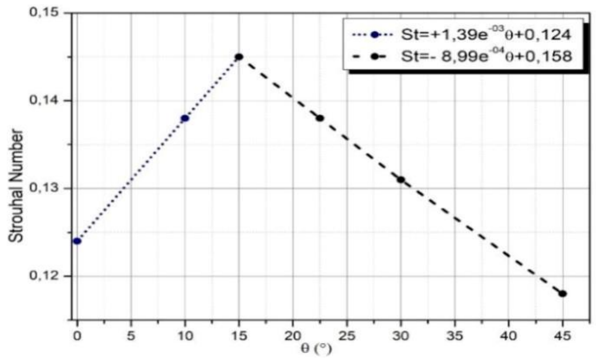

Fig. 13: Strouhal number versus obstacle inclination
Source: created by the authors

4 Conclusion

The impact of the obstacle's inclination angle on fluid dynamics is particularly important. The influence of obstacle inclination on turbulent flow behavior is investigated numerically using URANS turbulence models. Strouhal number for various angles of inclination varies linearly with the obstacle's inclination: it increases up to a critical angle of 15°, where it reaches its maximum, and then decreases beyond this angle. The present study shows that the case of obstacle inclination θ=15° corresponds to a maximal asymmetry and deformation of the flow downstream of the obstacle, due to the most pronounced boundary layer separation. It corresponds to a critical point where turbulence and vortex intensity are optimal. On the other hand, the 45° angle seems to be the most favorable, characterized by the minimal pressure and intense recirculation zones, leading to a transition toward a more stable flow.

These results may be considered in industrial implications, particularly in the design of aerodynamic and marine devices.

Nomenclature

C_L	Lift coefficient
f (Hz)	Frequency of the lift force
L (m)	Channel length
H (m)	Channel height
h (m)	Side length of the square obstacle
k (m^2/s^2)	Kinetic energy
St	Strouhal number ($f \cdot h/U_b$)
U_m (m/s)	Mean inlet velocity
U_i(m/s)	Mean velocity components
U_b (m/s)	Mean velocity at the cylinder location
$\overline{u_i u_j}$ (m^2/s^2)	Stress tensor
θ (°)	Inclination angles
ω (s^{-1})	Specific rate of dissipation of k

Declaration of Generative AI and AI-assisted Technologies in the Writing Process
The authors wrote, reviewed and edited the content as needed and verifies that none utilized artificial intelligence (AI) tools were used. The authors take full responsibility for the content of the publication.

References:

[1] Martínez-Sánchez, Á., López, E., Le Clainche, S., Lozano-Durán, A., Srivastava, A., & Vinuesa, R. (2023). Causality analysis of large-scale structures in the flow around a wall-mounted square cylinder. *Journal of Fluid Mechanics*, 967, A1. https://doi:10.1017/jfm.2023.423.

[2] Seyed M. Hajimirzaie. (2023). Experimental observations on flow characteristics around a low-aspect-ratio wall-mounted circular and square cylinder. *Fluids*, 8(1), 32. https://doi.org/10.3390/fluids8010032.

[3] Brahimi, A., Rebhi, R., & Alliche, M. (2023). Numerical Study of the Effects of Roughness Coupled with Inclination on a Turbulent Flow around an Obstacle. *Processes*, 11(7), 1979. https://doi.org/10.3390/pr11071979.

[4] Aly, A. M. (2024). Deep Learning-Based Eddy Viscosity Modeling for Improved RANS Simulations of Wind Pressures on Bluff Bodies. *Journal of Applied Fluid Mechanics*, 17(12), 2514-2532. https://doi.org/10.47176/jafm.17.12.2770.

[5] Nakagawa, S., Nitta, K., & Senda, M. (1999). An experimental study on unsteady turbulent near wake of a rectangular cylinder in channel flow. *Experiments in Fluids*, 27(3), 284-294. https://doi.org/10.1007/s003480050353.

[6] Kim, D. H., Yang, K. S., & Senda, M. (2004). Large eddy simulation of turbulent flow past a square cylinder confined in a channel. *Computers & Fluids*, 33(1), 81-96. https://doi:10.1016/S0045-7930(03)00040-9.

[7] G. Filippini, G. Franck, N. Nigro, M. Storti, J. D'Elía. (2005, November). Congreso Argentino de Mecánica Computational, Buenos Aires, Argentina, *Mecánica Computacional*, Vol. XXIV, 1279–1298.

[8] Rodi, W., Ferziger, J. H., Breuer, M., & Pourquie, M. J. B. M. (1997). Status of large eddy simulation: results of a workshop. *Transactions-American Society of Mechanical Engineers Journal of Fluids Engineering*, *119*, 248-262. https://doi.org/10.1115/1.2819128.

[9] Becker, S., Lienhart, H., & Durst, F. (2002). Flow around three-dimensional obstacles in boundary layers. *Journal of Wind Engineering and Industrial Aerodynamics*, 90(4-5), 265-279. https://doi.org/10.1016/S0167-6105(01)00209-4.

[10] Cheng, Y., Lien, F. S., Yee, E., & Sinclair, R. (2003). A comparison of large Eddy simulations with a standard k–ε Reynolds-averaged Navier–Stokes model for the prediction of a fully developed turbulent flow over a matrix of cubes. *Journal of Wind Engineering and Industrial Aerodynamics*, 91(11), 1301-1328. https://doi.org/10.1016/j.jweia.2003.08.001.

[11] Talbi, K., and EL-Houas Bedjeghit. "*Étude expérimentale et numérique d'un écoulement autour d'obstacles carré et cylindrique*." (2010).

[12] Xu, F. Y., Ying, X. Y., & Zhang, Z. (2011). Prediction of unsteady flow around a square cylinder using RANS. *Applied Mechanics and Materials*, 52, 1165-1170. https://doi.org/10.4028/www.scientific.net/AMM.52-54.1165.

[13] Yoon, D. H., Yang, K. S., & Choi, C. B. (2010). Flow past a square cylinder with an angle of incidence. *Physics of Fluids*, 22(4). https://doi.org/10.1063/1.3388857.

[14] Benahmed, L., & Aliane, K. (2019). Simulation and analysis of a turbulent flow around a three-dimensional obstacle. Acta Mechanica et Automatica, 13(3). https://doi.org/10.2478/ama-2019-0023.

[15] Jones, W. P., & Launder, B. E. (1972). The prediction of laminarization with a two-equation model of turbulence. *International Journal of Heat and Mass Transfer*, 15(2), 301-314. https://doi.org/10.1016/0017-9310(72)90076-2.

[16] Menter, F. (1993, July). Zonal two equation k–ω turbulence models for aerodynamic flows. In *23rd Fluid Dynamics, Plasma dynamics, and Lasers Conference* (p. 2906). https://doi.org/10.2514/6.1993-2906.

[17] Wilcox, D. C. (1988). Reassessment of the scale-determining equation for advanced turbulence models. *AIAA Journal*, 26(11), 1299-1310. https://doi.org/10.2514/3.10041.

[18] B. Launder, G. J. Reece, W. Rodi, Progress in the Development of a Reynolds Stress Turbulence Closure, *Journal of Fluid Mechanics*, Vol. 68, No. 3, 1975, pp. 537–566. https://doi.org/10.1017/S0022112075001814.

[19] S.V. Patankar, *Numerical Heat Transfer and Fluid Flow*, Taylor & Francis Publishers, New York, 1980. https://doi.org/10.1201/9781482234213.

[20] F. Nieto, D. Hargreaves, J.S. Owen, S. Hernandez, On the Applicability of 2D URANS and SST-(k–ω) Turbulence Model to the Fluid-Structure Interaction of Rectangular Cylinders, Engineering Applications of Computational Fluid Mechanics, *Taylor & Francis*, Vol. 9, No. 1, 2015, pp. 1–17. https://doi.org/10.1080/19942060.2015.1004817.

Contribution of Individual Authors to the Creation of a Scientific Article (Ghostwriting Policy)

- Nora Bensider was responsible for the entirety of the work, including the conceptualization, methodology, simulation, validation, analysis, and manuscript preparation.
- Amina Mataoui contributed by reviewing the manuscript and providing critical feedback and editorial suggestions.
- Samira Louaifi participated in the revision of the entire manuscript.

Sources of Funding for Research Presented in a Scientific Article or Scientific Article Itself

No funding was received for conducting this study.

Conflicts of Interest

The authors have no conflicts of interest to declare

APPENDIX

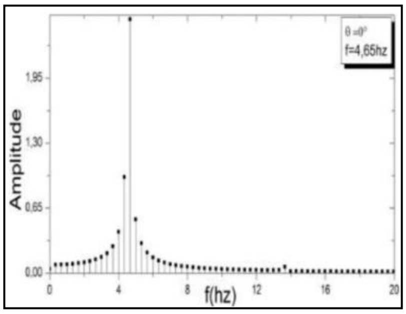

(a) $\theta = 0°$

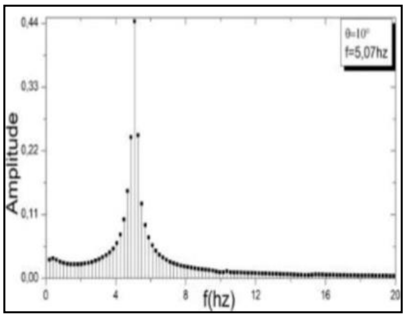

(b) $\theta = 10°$

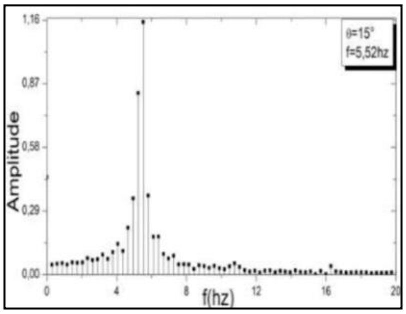

(c) $\theta = 15°$

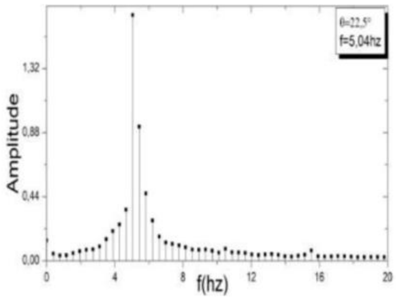

(d) $\theta = 22.5°$

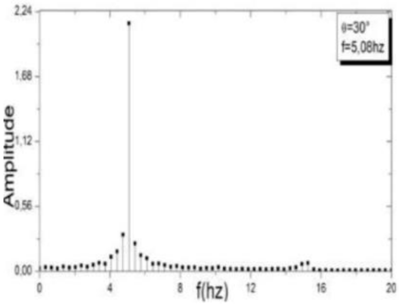

(e) $\theta = 30°$

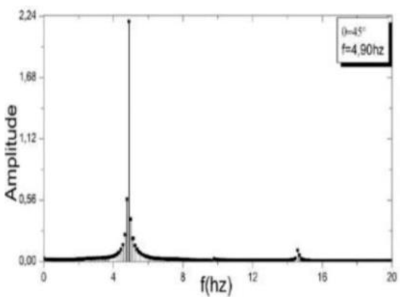

(f) $\theta = 45°$

Fig. 11: The frequency based on the lift force for each obstacle inclination

Source: created by the authors

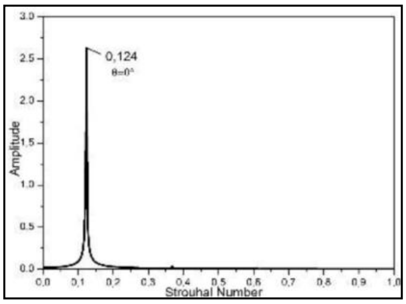

(a) $\theta = 0°$

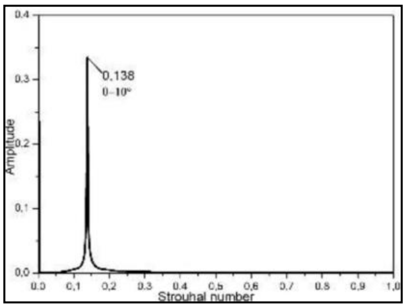

(b) $\theta = 10°$

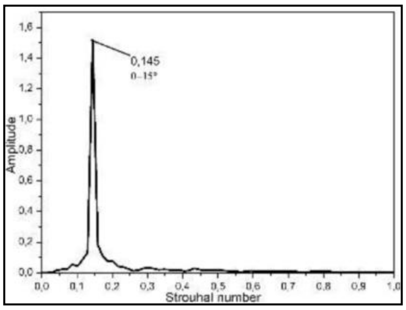

(c) $\theta = 15°$

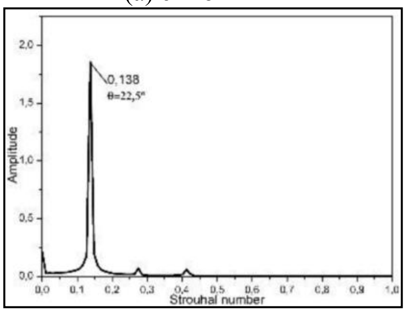

(d) $\theta = 22.5°$

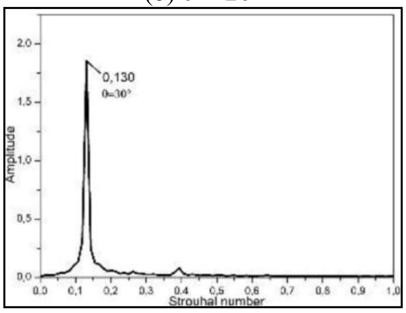

(e) $\theta = 30°$

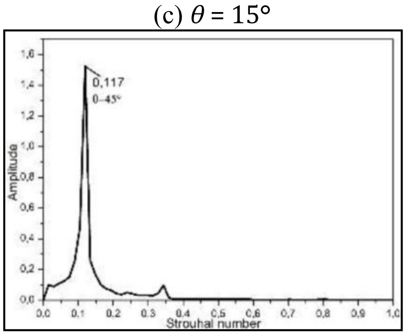

(f) $\theta = 45°$

Fig. 12: Strouhal number for each obstacle inclination

Source: created by the authors